Geometrically non-linear multi-layer beam with interconnection allowing for mixed-mode delamination

Leo Škec[a], Gordan Jelenić[a,*]

[a]*Faculty of Civil Engineering, University of Rijeka, Radmile Matejčić 3, 51000 Rijeka, Croatia*

Abstract

In this work we assess the extent to which a beam model is suitable for the finite-element analysis of composite structures undergoing a large-displacement delamination process. We lay down the necessary theory needed for the geometrically non-linear analysis using Reissner's beam theory for the layers to be applied to layered structures involving dual-mode damage-type bi-linear constitutive law for the interconnections, run a number of representative examples and compare the results to those obtained using a geometrically linear analysis. The formulation is given in a general form where the number of layers and nodes of the beam finite elements is arbitrary. To solve numerical problems, the equilibrium of which is necessarily more complex and demanding to satisfy than in the geometrically linear case, the standard cylindrical arc-length procedure is used only when there is no damage at the interconnection. When damage at the interconnection occurs, the standard arc-length method has been modified so that in each load step the converged solution is required to result in an increase in the total damage of the system. It is concluded that the geometrically linear formulations can be used with satisfactory accuracy only in limited number of cases where displacements and rotations remain small.

Keywords: multi-layered structure, mixed-mode delamination, bilinear damage law, non-linear analysis, multi-layered beam finite element

*Corresponding author
Email address: gordan.jelenicuniri.hr (Gordan Jelenić)

1. Introduction

Structures composed of multiple layers can be found in many areas of engineering as well as in nature. The most prevalent failure mechanism of such structures is delamination in which the connection between the layers is being progressively damaged due to cracking and is eventually completely lost. Obviously, this failure mechanism is very complex for a variety of reasons.

To start with, it exhibits overall structural softening upon reaching a particular strength of the interconnection [1] and in order to assess this strength it becomes necessary to invoke the fundamental energy principles from the theory of fracture mechanics [2]. The actual softening may be described exponentially, as in the linear fracture mechanics (see e.g. [3]) or as a linear or multi-linear curve, often used in numerical analyses. The global manifestation of post-critical softening may often become apparent in considerably larger overall displacements compared to those in the pre-critical range necessitating a geometrically non-linear structural analysis.

In addition, instead of considering the delamination stress at the crack tip as infinite, which follows from the principles of linear fracture mechanics [4], in real practical problems it becomes necessary to recognise that the fracturing process is governed by a finite stress distribution over a small region around the crack tip, the so-called "process zone" in Barenblatt's cohesive zone models (CZM) [5]. The cohesive zone models enable the stresses to 'straddle' a narrow crack and describe a variety of physical phenomena rather well, from generation and localisation of a principal crack [6, 7, 8] to aggregate interlocking in concrete structures [9].

Also, a crack between two layers may occur for different reasons leading to the so-called Mode I, II or III openings (normal to the crack surface, or tangential to it due to slippage or tearing) [1]. Obviously, these may not be considered separately since even a limited damage in a particular mode always comes as a consequence of some underlying physical re-arrangement of particle bonds on a sufficiently small scale which necessarily reduces also the strengths

in the other modes. It thus becomes necessary to define a certain scalar measure of overall damage (see e.g. [10]), which involves contribution from all possible modes and governs the phenomenon of damage-induced strength reduction in all the modes.

When modelling engineering problems we are naturally led by the demands of (i) accuracy and (ii) computational efficience, which need to be met to within a prescribed measure and in some sense optimised. For the class of problems analysed here, in our previous work [11] it has been shown that using beam finite elements instead of 2D solids for planar geometrically linear delamination gives results of comparable accuracy using significantly less degrees of freedom. Such elements do not appear to be as wide-spread in this type of analysis as the solids, and it is thus argued that they should be considered as a valid alternative in a variety of situations, including mixed-mode delamination. The efficiency of multi-layer beam finite elements in comparison with commonly used 2D solids has been shown also in authors' previous work [12] where the connection between the layers was assumed to be absolutely rigid (see also [13] and [14]).

In this work we attempt to assess the extent to which the beam model and, more generally the geometrically linear set-up itself, are applicable to the analysis of the composite structures undergoing a delamination process. Not unexpectedly, such structures are usually designed to take advantage of the particular properties of the materials forming the composite without being damaged in the operational state. However, if we want to trace the post-critical equilibrium path after the process of delamination has initiated, possibly all the way up to full rupture, we have to recognise that the ratio between the displacement and the loading magnitudes may increase considerably. There also exist such delamination phenomena, e.g. peeling, in which the displacements are of the order of magnitude of the geometry of the problem analysed.

In such situations, obviously, geometrically linear analysis may not return the results representative of the real behaviour of the problem analysed. Given the complexity of the delamination process, it is not always possible to tell in advance if the geometrically non-linear effects may not in fact become consider-

able even for deformation magnitudes which we may be tempted to intuitivelly classify as 'small'.

In this work we will lay down the necessary theory needed for the geometrically non-linear analysis using Reissner's beam theory for the layers to be applied to layered structures involving dual-mode damage-type bi-linear constitutive law for the interconnections. In order to assess the need for the geometrically non-linear analysis presented, we will run a number of representative examples and compare the results to those obtained using a geometrically linear analysis.

2. Problem description

Geometry of deformation of a multi-layer beam is described in [11] and here we reproduce it for reference. An initially straight multi-layer beam composed of n layers and $n-1$ interconnections is considered. An arbitrary interconnection α is placed between layers i and $i+1$.

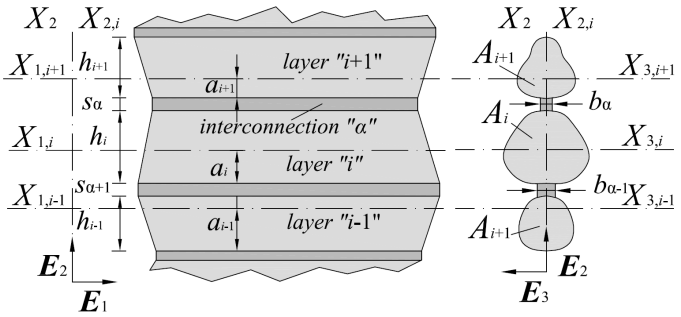

Figure 1: Position of a segment of a multi-layer beam with interconnection in the material co-ordinate system

Material co-ordinate system of each layer is defined by an orthonormal triad of vectors $\boldsymbol{E}_{1,i}$, $\boldsymbol{E}_{2,i}$, $\boldsymbol{E}_{3,i}$, with axes $X_{1,i}, X_{2,i}, X_{3,i}$ (see Fig. 1). The axes $X_{1,i}$ are parallel with the layer's edges and mutually ($\boldsymbol{E}_1 = \boldsymbol{E}_{1,i}$ and $X_1 = X_{1,i}$) coincide with the reference axes of each layer. The position of a reference axis over the layer's height $a_i \in \langle 0, h_i \rangle$ may be chosen arbitrarily, where h_i is the layer's height. However, in [11] it was shown that the position of the reference

axis may influence the numerical results. The cross-sections of all layers have a common vertical principal axis X_2 defined by a base vector $\boldsymbol{E}_2 = \boldsymbol{E}_{2,i}$ (a condition for a planar deformation). Note that, according to Fig. 1, the co-ordinate $X_{2,i}$ is different for each layer i. Axes $X_{3,i}$ are mutually parallel ($X_3 = X_{3,i}$ and $\boldsymbol{E}_3 = \boldsymbol{E}_{3,i}$), but they do not necessarily coincide with the horizontal principal axes of the layers' cross-sections. The first and the second moment of area of the layer's cross-section with respect to axis $X_{3,i}$ are defined as

$$S_i = \int_{A_i} X_{2,i} \mathrm{d}A, \quad I_i = \int_{A_i} (X_{2,i})^2 \mathrm{d}A, \tag{1}$$

where A_i is the area of the cross-section of the layer. In our model it is assumed that the thickness of the interconnection is very small compared to the layers' thicknesses, i.e. the geometry of an interconnection α is completely defined by its height and width, denoted as s_α and b_α, respectively.

The direction of reference axes of all the layers in the initial undeformed state is defined by the unit vector $\boldsymbol{t}_{01}$ which closes an angle ψ with respect to the axis defined by the base vector $\boldsymbol{e}_1$ of the spatial co-ordinate system (see Fig. 2). Vector $\boldsymbol{t}_{02}$ defines the orientation of layers' cross-sections which are orthogonal to the layers' reference axes. Thus, the following relationship can be established:

$$\boldsymbol{t}_{0j} = \boldsymbol{\Lambda}_0 \boldsymbol{e}_j = \begin{bmatrix} \cos\psi & -\sin\psi \\ \sin\psi & \cos\psi \end{bmatrix} \boldsymbol{e}_j, \text{ where } j = 1, 2. \tag{2}$$

According to Fig. 2, the position of a material point in the layer i, $T(X_1, X_{2,i})$ in the undeformed state is defined by the vector

$$\boldsymbol{x}_{0,i}(X_1, X_{2,i}) = \boldsymbol{r}_{0,i}(X_1) + X_{2,i}\boldsymbol{t}_{02}, \tag{3}$$

where $\boldsymbol{r}_{0,i}(X_1)$ is the position of the intersection of the plane of the cross-section containing the point T and the reference axis of the layer i in the undeformed state. The cross-sections of the layers remain planar but not necessarily

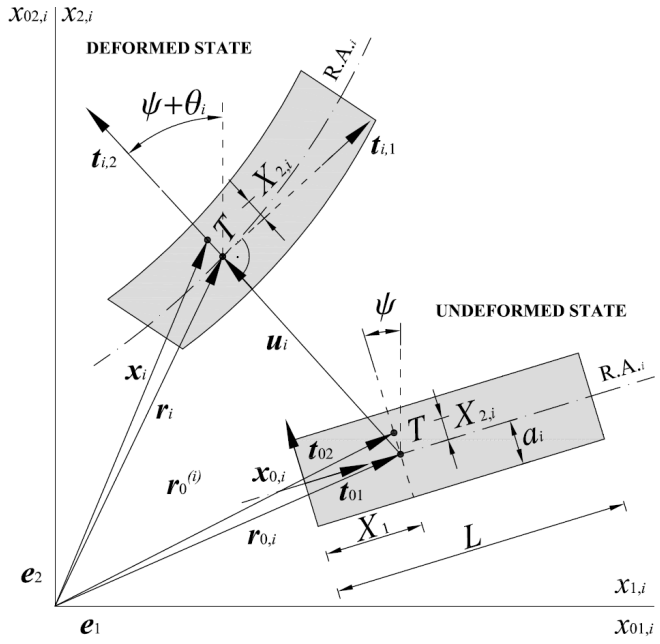

Figure 2: Position of a layer of the composite beam in the spatial co-ordinate systam in the undeformed and a deformed state

orthogonal to their reference axes during the deformation of the beam (Timoshenko beam theory with the Bernoulli hypothesis) and the material base vector $\boldsymbol{E}_3$ remains orthogonal to the plane spanned by the spatial base $\boldsymbol{e}_1$ and $\boldsymbol{e}_2$. Orientation of the cross-section of layer i in the deformed state is defined by the base vectors

$$\boldsymbol{t}_{i,j} = \begin{bmatrix} \cos(\psi+\theta_i) & -\sin(\psi+\theta_i) \\ \sin(\psi+\theta_i) & \cos(\psi+\theta_i) \end{bmatrix} \boldsymbol{e}_j = \boldsymbol{\Lambda}_i \boldsymbol{e}_j, \text{ where } j = 1, 2. \tag{4}$$

Rotation of the cross-section of layer i is denoted as θ_i and it is entirely dependent on X_1, thus $\theta_i = \theta_i(X_1)$. The position of material point T in the deformed state can be thus expressed as

$$\boldsymbol{x}_i(X_1, X_{2,i}) = \boldsymbol{r}_i(X_1) + X_{2,i}\boldsymbol{t}_{i,2}(X_1), \tag{5}$$

where $\boldsymbol{r}_i(X_1)$ is the position of the intersection of the plane of the cross-section containing the point T and the reference axis of layer i in the deformed state. Thus, the displacement between the deformed and the undeformed reference axis can be defined for each layer as

$$\boldsymbol{u}_i(X_1) = \boldsymbol{r}_i(X_1) - \boldsymbol{r}_{0,i}(X_1). \tag{6}$$

3. Governing equations

The first group of governing equations defines how the layers and the interconnections are assembled into a multi-layer beam. The kinematic, constitutive and equilibrium equations are then defined for the layers, as well as for the interconnections.

3.1. Assembly equations

A segment of the multi-layer beam is shown in Fig. 3 in its undeformed and deformed state.

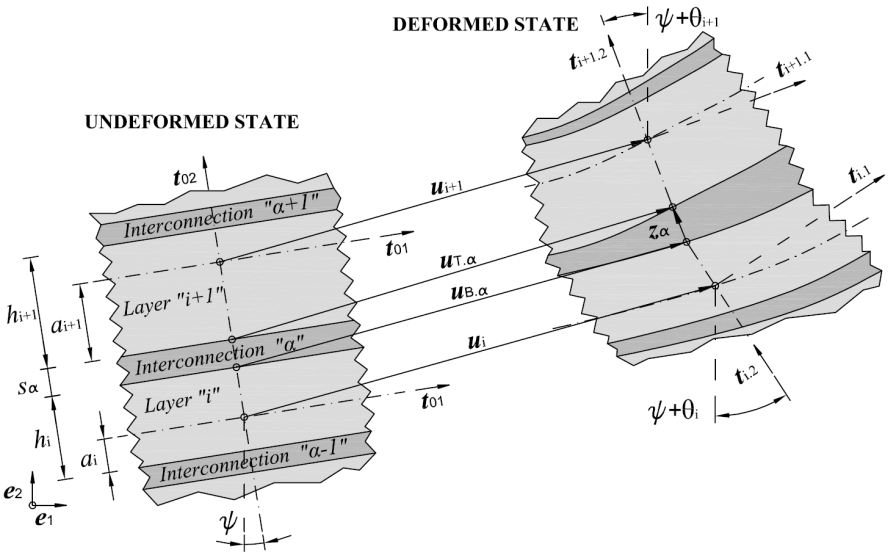

Figure 3: Undeformed and deformed state of a segment of a multi-layer beam with interconnection

To define relative displacement between layers i and $i+1$ at interconnection α it is necessary to define the displacements at the top and the bottom of the interconnection as

$$\boldsymbol{u}_{T,\alpha} = \boldsymbol{u}_{i+1} + (\boldsymbol{t}_{02} - \boldsymbol{t}_{i+1,2})a_{i+1}, \tag{7}$$

$$\boldsymbol{u}_{B,\alpha} = \boldsymbol{u}_{i} + (\boldsymbol{t}_{i,2} - \boldsymbol{t}_{02})(h_i - a_i), \tag{8}$$

Vector $\boldsymbol{z}_\alpha$, which represents a directed stretched thickness of interconnection α, can be expressed according to Fig. 3 using (7) and (8) as

$$\begin{aligned}\boldsymbol{z}_\alpha &= s_\alpha \boldsymbol{t}_{02} + \boldsymbol{u}_{T,\alpha} - \boldsymbol{u}_{B,\alpha} = \\ &= \boldsymbol{u}_{i+1} - \boldsymbol{u}_i + a_{i+1}(\boldsymbol{t}_{02} - \boldsymbol{t}_{i+1,2}) + (h_i - a_i)(\boldsymbol{t}_{02} - \boldsymbol{t}_{i,2}) + s_\alpha \boldsymbol{t}_{02}.\end{aligned} \tag{9}$$

3.2. Governing equations for layers

Governing equations for each layer consist of kinematic, constitutive and equilibrium equations.

3.2.1. Kinematic equations

The kinematic equations are the exact non-linear equations according to Reissner's beam theory [15] and notation introduced by Simo & Vu-Quoc [16]:

$$\boldsymbol{\gamma}_i = \begin{Bmatrix} \epsilon_i \\ \gamma_i \end{Bmatrix} = \boldsymbol{\Lambda}_i^{\mathsf{T}} \boldsymbol{r}_i' - \boldsymbol{E}_1 = \boldsymbol{\Lambda}_i^{\mathsf{T}} (\boldsymbol{t}_{01} + \boldsymbol{u}_i') - \boldsymbol{E}_1, \tag{10}$$

$$\kappa_i = \theta_i', \tag{11}$$

where $\epsilon_i, \gamma_i, \kappa_i$ are the axial, shear and rotational strain (infinitesimal change of the cross-sectional rotation) at the reference axis of layer i, respectively. Since these quantities are functions of only X_1, the differentiation with respect to X_1 is introduced and denoted as $(\bullet)'$.

3.2.2. Constitutive equations

In this work the layers are assumed do be made of linear elastic material with E_i and G_i as Young's and shear moduli of each layer's material. The axial strain of a fibre at the distance $X_{2,i}$ from the reference axis of the layer i can be computed as

$$\varepsilon_i = \varepsilon_i(X_1, X_{2,i}) = \epsilon_i(X_1) - X_{2,i}\kappa_i(X_1), \tag{12}$$

where $\epsilon_i(X_1)$ is the axial strain of a fibre at the layer's reference axis. For the linear elastic material the normal stress follows as

$$\sigma_i = \sigma_i(X_1, X_{2,i}) = E_i\varepsilon_i(X_1, X_{2,i}), \tag{13}$$

while the shear stress is assumed to be constant over the cross section ($T_i = G_i\gamma_i$). From (12) and (13), in contrast, it can be clearly noted that the distribution of normal stresses over the layer's height is linear. The stress resultants then read

$$N_i = \int_{A_i} \sigma_i \mathrm{d}A, \tag{14}$$

$$T_i = G_i k_i A_i \gamma_i, \tag{15}$$

$$M_i = -\int_{A_i} X_{2,i}\sigma_i \mathrm{d}A, \tag{16}$$

where N_i, T_i, M_i are the axial force, shear force and bending moment with respect to the reference axis of layer i, respectively. The shear correction coefficient for layer i comes as a consequence of the assumption of constant shear over the cross section introduced earlier and is denoted as k_i [17]. Substituting (12) and (13) in (14)-(16) we finally obtain

$$\begin{Bmatrix} \boldsymbol{N}_i \\ M_i \end{Bmatrix} = \boldsymbol{C}_i \begin{Bmatrix} \boldsymbol{\gamma}_i \\ \kappa_i \end{Bmatrix}, \tag{17}$$

where $\boldsymbol{N}_i^{\mathsf{T}} = \langle N_i \; T_i \rangle^{\mathsf{T}}$, $\boldsymbol{\gamma_i}^{\mathsf{T}} = \langle \varepsilon_i \; \gamma_i \rangle^{\mathsf{T}}$ and

$$\boldsymbol{C}_i = \begin{bmatrix} E_i A_i & 0 & -E_i S_i \\ 0 & G_i k_i A_i & 0 \\ -E_i S_i & 0 & E_i I_i \end{bmatrix} \tag{18}$$

is the constitutive matrix of layer i.

3.2.3. Equilibrium equations

3.2.3.1 Continuous form. Equilibrium equations for layer i are derived from the principle of virtual work, where the total virtual work of the layer V_i^L is the difference between the virtual work of internal forces V_i^{int} and the virtual work of external forces V_i^{ext} acting on layer i. This can be written as

$$\begin{aligned} V_i^L \equiv & V_i^{int} - V_i^{ext} = \int_0^L \left(\overline{\boldsymbol{\gamma}}_i \cdot \boldsymbol{N}_i + \overline{\kappa}_i M_i\right) \mathrm{d}X_1 - \int_0^L \left(\overline{\boldsymbol{u}}_i \cdot \boldsymbol{f}_i + \overline{\theta}_i w_i\right) \mathrm{d}X_1 - \\ & - \overline{\boldsymbol{u}}_i(0) \cdot \boldsymbol{F}_{i,0} - \overline{\theta}_i(0) W_{i,0} - \overline{\boldsymbol{u}}_i(L) \cdot \boldsymbol{F}_{i,L} - \overline{\theta}_i(L) W_{i,L}, \end{aligned} \tag{19}$$

where $\overline{\boldsymbol{\gamma}}_i$ and $\overline{\kappa}_i$ are the virtual strains, while $\overline{\boldsymbol{u}}_i$ and $\overline{\theta}_i$ denote the virtual displacements and rotations, which are all functions of X_1. The distributed external forces and moments over the beam's length are denoted as $\boldsymbol{f}_i$ and w_i, while the corresponding point loads concentrated on the beam ends are denoted as $\boldsymbol{F}_{i,0}$, $W_{i,0}$, $\boldsymbol{F}_{i,L}$, $W_{i,L}$. The virtual strains are the linear parts of the strains in (10) and (11) with respect to the (virtual) displacements and rotations and can be expressed as

$$\begin{Bmatrix} \overline{\boldsymbol{\gamma}}_i \\ \overline{\kappa}_i \end{Bmatrix} = \begin{bmatrix} \boldsymbol{\Lambda}_i^{\mathsf{T}} & \boldsymbol{0} \\ \boldsymbol{0}^{\mathsf{T}} & 1 \end{bmatrix} \left(\begin{bmatrix} \boldsymbol{I}_2 \frac{\mathrm{d}}{\mathrm{d}X_1} & -\hat{\boldsymbol{t}}_3(\boldsymbol{t}_{01} + \boldsymbol{u}_i') \\ \boldsymbol{0}^{\mathsf{T}} & \frac{\mathrm{d}}{\mathrm{d}X_1} \end{bmatrix} \begin{Bmatrix} \overline{\boldsymbol{u}}_i \\ \overline{\theta}_i \end{Bmatrix} \right) = \boldsymbol{L}_i(\boldsymbol{D}_i \overline{\boldsymbol{p}}_i), \tag{20}$$

where $\boldsymbol{0} = \{0 \quad 0\}^{\mathsf{T}}$, $\boldsymbol{I}_2$ is a 2×2 identity matrix and $\hat{\boldsymbol{t}}_3 = \begin{bmatrix} 0 & -1 \\ 1 & 0 \end{bmatrix}$.

Expression (19) now becomes

$$V_i^L = \int_0^L \left[(\boldsymbol{D}_i \overline{\boldsymbol{p}}_i)^\mathsf{T} \boldsymbol{L}_i^\mathsf{T} \begin{Bmatrix} \boldsymbol{N}_i \\ M_i \end{Bmatrix} - \overline{\boldsymbol{p}}_i^\mathsf{T} \begin{Bmatrix} \boldsymbol{f}_i \\ w_i \end{Bmatrix} \right] \mathrm{d}X_1 - \overline{\boldsymbol{p}}_i^\mathsf{T}(0) \begin{Bmatrix} \boldsymbol{F}_{i,0} \\ W_{i,0} \end{Bmatrix} - \overline{\boldsymbol{p}}_i^\mathsf{T}(L) \begin{Bmatrix} \boldsymbol{F}_{i,L} \\ W_{i,L} \end{Bmatrix}. \tag{21}$$

3.2.3.2 Discrete form. The resulting expression is highly non-linear in terms of the basic unknown functions ($\boldsymbol{u}_i$ and θ_i) and eventually leads to equilibrium which cannot be found in a closed form. Thus, the shape of the virtual (test) functions ($\overline{\boldsymbol{u}}_i$ and $\overline{\theta}_i$) is chosen in advance assuming that for a finite number of nodes N on a finite element the virtual displacements and rotations are known at the nodes ($\overline{\boldsymbol{u}}_{i,j}$ and $\overline{\theta}_{i,j}$, $j \in \{1, N\}$) and interpolated between them as

$$\overline{\boldsymbol{p}}_i \doteq \sum_{j=1}^{N} \boldsymbol{\Psi}_j(X_1) \begin{Bmatrix} \overline{\boldsymbol{u}}_{i,j} \\ \overline{\theta}_{i,j} \end{Bmatrix} = \sum_{j=1}^{N} \boldsymbol{\Psi}_j(X_1) \overline{\boldsymbol{p}}_{i,j}, \tag{22}$$

where $\boldsymbol{\Psi}_j$ is a 3×3 matrix of interpolation functions. If we further introduce the nodal global vector of virtual unknown parameters $\overline{\boldsymbol{p}}_{G,j} = \langle \overline{\boldsymbol{p}}_{1,j} \quad \overline{\boldsymbol{p}}_{2,j} \quad \dots \overline{\boldsymbol{p}}_{n,j} \rangle^\mathsf{T}$ for all the layers in the finite element, we can write

$$\overline{\boldsymbol{p}}_i = \sum_{j=1}^{N} \begin{bmatrix} \delta_{i1}\boldsymbol{\Psi}_j & \delta_{i2}\boldsymbol{\Psi}_j & \dots & \delta_{in}\boldsymbol{\Psi}_j \end{bmatrix} \overline{\boldsymbol{p}}_{G,j} = \sum_{j=1}^{N} \boldsymbol{P}_{i,j} \overline{\boldsymbol{p}}_{G,j}, \tag{23}$$

where δ_{ij} is the Kronecker delta defined as

$$\delta_{ij} = \begin{cases} 1 & \text{if } i = j, \\ 0 & \text{otherwise.} \end{cases} \tag{24}$$

At this point, expression (21) can be written as

$$V_i^L = \sum_{j=1}^{N} \overline{\boldsymbol{p}}_{G,j}^\mathsf{T} \left\{ \int_0^L \left[(\boldsymbol{D}_i \boldsymbol{P}_{i,j})^\mathsf{T} \boldsymbol{L}_i^\mathsf{T} \begin{Bmatrix} \boldsymbol{N}_i \\ M_i \end{Bmatrix} - \boldsymbol{P}_{i,j}^\mathsf{T} \begin{Bmatrix} \boldsymbol{f}_i \\ w_i \end{Bmatrix} \right] \mathrm{d}X_1 - \right.$$
$$\left. - \boldsymbol{P}_{i,j}^\mathsf{T}(0) \begin{Bmatrix} \boldsymbol{F}_{i,0} \\ W_{i,0} \end{Bmatrix} - \boldsymbol{P}_{i,j}^\mathsf{T}(L) \begin{Bmatrix} \boldsymbol{F}_{i,L} \\ W_{i,L} \end{Bmatrix} \right\} = \sum_{j=1}^{N} \overline{\boldsymbol{p}}_{G,j}^\mathsf{T} \boldsymbol{g}_{i,j}^L, \tag{25}$$

where $\boldsymbol{g}_{i,j}^{L}$ (the term within the braces of (25)) is the nodal vector of residual forces for the layer i which will be later introduced to the global equilibrium equation of the multi-layer beam with interconnection. It should be noted that $\boldsymbol{D}_i$ and $\boldsymbol{L}_i$ now depend on the current configuration (see (20)), in contrast to the procedure given in [11]. This is where the geometric non-linearity of the layers' deformation is accounted for.

3.3. Governing equations for interconnections

Each interconnection allows for delamination in single modes (I and II), as well as for the mixed-mode delamination. Non-linear constitutive law with the embedded cohesive zone model (CZM) [10] is assumed for directions corresponding to modes I and II. Mixed-mode delamination is determined by combining the influence of individual modes. The governing equations for each interconnection again consist of kinematic, constitutive and equilibrium equations.

3.3.1. Kinematic equations

In order to determine the delamination in individual modes, first we have to define the directions corresponding to modes I and II. In case of large displacements and rotations defining tangential and normal separation at the interconnection is not unique and may be defined in a number of ways. The line along which tangential separation between layers (mode II delamination) occurs lays somewhere between the tangent to the reference axes of layers i and $i+1$ and can be defined by the angle

$$\theta_{\alpha}^{m} = \zeta(\psi + \theta_i) + (1-\zeta)(\psi + \theta_{i+1}) = \psi + \zeta\theta_i + (1-\zeta)\theta_{i+1}, \tag{26}$$

where ζ represents the weight with a value between 0 and 1. In the present work value $\zeta = 0.5$ has been used in all numerical examples. Analysis of the impact of coefficient ζ on the results has been performed in [18] and it has been shown there that variation of ζ between 0 and 1 has a small influence on the results for the examples analysed there. The relative displacements at

interconnection α according to (9) can be now decomposed in two directions corresponding to delamination modes I and II and written in a vector as

$$\boldsymbol{d}_\alpha = \begin{Bmatrix} d_{1,\alpha} \\ d_{2,\alpha} \end{Bmatrix} = \boldsymbol{\Lambda}_\alpha^m (\boldsymbol{z}_\alpha - s_\alpha \boldsymbol{t}_{02}) = \boldsymbol{\Lambda}_\alpha^m (\boldsymbol{u}_{T,\alpha} - \boldsymbol{u}_{B,\alpha}), \tag{27}$$

where

$$\boldsymbol{\Lambda}_\alpha^m = \begin{bmatrix} \cos\theta_\alpha^m & -\sin\theta_\alpha^m \\ \sin\theta_\alpha^m & \cos\theta_\alpha^m \end{bmatrix}. \tag{28}$$

Note that index 1 corresponds to mode II and index 2 to mode I delamination.

3.3.2. Constitutive equations

For an arbitrary interconnection α the constitutive law for the directions corresponding to delamination modes I and II is shown in Fig. 4. This concept was proposed by Alfano and Crisfield [10] who used the so-called interface finite elements with embedded cohesive zone model (CZM).

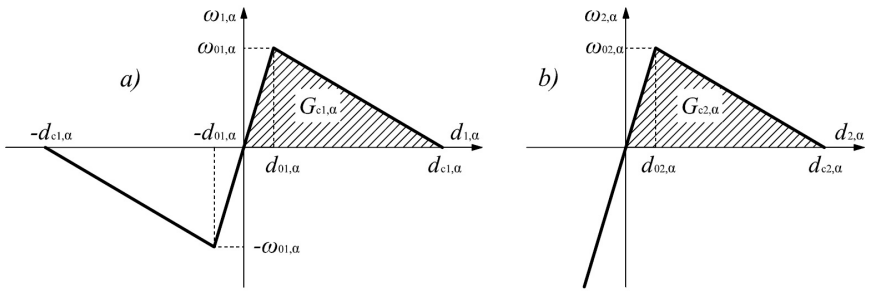

Figure 4: Constitutive law for the interconnection: a) mode II (direction 1) and b) mode I (direction 2)

The current state of damage is defined using a parameter which combines delamination in both modes as

$$\beta_\alpha(\tau') = \left[\left(\frac{|d_{1,\alpha}(\tau')|}{d_{01,\alpha}} \right)^\eta + \left(\frac{\langle d_{2,\alpha}(\tau') \rangle}{d_{02,\alpha}} \right)^\eta \right]^{\frac{1}{\eta}} - 1, \tag{29}$$

where $d_{01,\alpha}$ and $d_{02,\alpha}$ are the relative displacements at the interconnection α at the start of the softening process in modes II and I (directions 1 and 2), respectively, τ' is the pseudo-time variable and $\langle\bullet\rangle$ is the McCauley bracket [10]. In all numerical examples in the present work $\eta = 2$ is used. The maximum rate of delamination in the pseudo-time history

$$\overline{\beta}_\alpha(\tau) = \max_{0\leq\tau'\leq\tau} \beta_\alpha(\tau') \tag{30}$$

ensures that the damage of the interconnection is irreversible. The tractions at the interconnection $\boldsymbol{\omega}_\alpha = \langle \omega_{\alpha,1} \quad \omega_{\alpha,2} \rangle^{\mathsf{T}}$ are obtained from the following constitutive law:

$$\boldsymbol{\omega}_\alpha = \begin{cases} \boldsymbol{S}_\alpha \boldsymbol{d}_\alpha & \text{if } \overline{\beta}_\alpha \leq 0, \\ \left[\boldsymbol{I} - \boldsymbol{G}_\alpha\right] \boldsymbol{S}_\alpha \boldsymbol{d}_\alpha & \text{if } \overline{\beta}_\alpha > 0, \end{cases} \tag{31}$$

where

$$\boldsymbol{S}_\alpha = \begin{bmatrix} S_{1,\alpha} & 0 \\ 0 & S_{2,\alpha} \end{bmatrix}, \quad S_{i,\alpha} = \frac{\omega_{0i,\alpha}}{d_{0i,\alpha}}, \quad \boldsymbol{G}_\alpha = \begin{bmatrix} g_{1,\alpha} & 0 \\ 0 & \langle \operatorname{sgn}(d_{2,\alpha}) \rangle g_{2,\alpha} \end{bmatrix},$$
$$g_{i,\alpha} = \min\left\{1, \frac{d_{ci,\alpha}}{d_{ci,\alpha} - d_{0i,\alpha}} \frac{\overline{\beta}_\alpha}{1 + \overline{\beta}_\alpha}\right\} \quad i = 1, 2, \tag{32}$$

$\omega_{0i,\alpha}$ is the contact traction at the interconnection α at the start of the softening process in direction i, while $d_{co,\alpha}$ represents the relative displacement corresponding to the total damage of the interconnection α in direction i. When $\overline{\beta}_\alpha \leq 0$ we have the linear-elastic behaviour of the interconnection, while $\overline{\beta}_\alpha > 0$ indicates the ongoing delamination and damage process at the interconnection. The degree of the damage is defined by the parameter $g_{i,\alpha} \in \langle 0, 1]$, where $g_{i,\alpha} = 1$ means that total damage of the interconnection has occurred and the connection between layers is completely lost ($\boldsymbol{\omega}_\alpha = \boldsymbol{0}$).

3.3.3. Equilibrium equations

3.3.3.1 Continuous form. Equilibrium equations for the interconnection can be derived from the principle of virtual work. It is assumed that no external loads

are applied directly on the interconnections and the virtual work of internal forces of the interconnection α reads

$$V_\alpha^C = b_\alpha \int_0^L \overline{\boldsymbol{d}}_\alpha \cdot \boldsymbol{\omega}_\alpha \mathrm{d}X_1. \tag{33}$$

From (27) it can be obtained

$$\overline{\boldsymbol{d}}_\alpha = \overline{\boldsymbol{\Lambda}}_\alpha^m (\boldsymbol{z}_\alpha - s_\alpha \boldsymbol{t}_{02}) + \boldsymbol{\Lambda}_\alpha^m \overline{\boldsymbol{z}}_\alpha \tag{34}$$

where

$$\begin{aligned}
\overline{\boldsymbol{\Lambda}}_\alpha^m =& \overline{\theta}_\alpha^m \hat{\boldsymbol{t}}_3 \boldsymbol{\Lambda}_\alpha^m, \\
\overline{\theta}_\alpha^m =& \{\boldsymbol{0}^\mathsf{T} \quad \zeta \quad \boldsymbol{0}^\mathsf{T} \quad (1-\zeta)\} \begin{Bmatrix} \overline{\boldsymbol{p}}_i \\ \overline{\boldsymbol{p}}_{i+1} \end{Bmatrix} = \boldsymbol{\varphi}^\mathsf{T} \overline{\boldsymbol{p}}_{C,\alpha}, \\
\overline{\boldsymbol{z}}_\alpha =& \begin{bmatrix} -\boldsymbol{I}_2 & \boldsymbol{t}_{i,1}(h_i - a_i) & \boldsymbol{I}_2 & \boldsymbol{t}_{i+1,1} a_{i+1} \end{bmatrix} \begin{Bmatrix} \overline{\boldsymbol{p}}_i \\ \overline{\boldsymbol{p}}_{i+1} \end{Bmatrix} = \boldsymbol{B}_\alpha \overline{\boldsymbol{p}}_{C,\alpha}.
\end{aligned} \tag{35}$$

Now, (34) becomes

$$\overline{\boldsymbol{d}}_\alpha = \left[\hat{\boldsymbol{t}}_3 \boldsymbol{\Lambda}_\alpha^m (\boldsymbol{z}_\alpha - s_\alpha \boldsymbol{t}_{02}) \boldsymbol{\varphi}^\mathsf{T} + \boldsymbol{\Lambda}_\alpha^m \boldsymbol{B}_\alpha\right] \overline{\boldsymbol{p}}_{C,\alpha} = \boldsymbol{Y}_\alpha \overline{\boldsymbol{p}}_{C,\alpha}. \tag{36}$$

3.3.3.2 Discrete form. Using

$$\overline{\boldsymbol{p}}_{C,\alpha} = \begin{Bmatrix} \overline{\boldsymbol{p}}_i \\ \overline{\boldsymbol{p}}_{i+1} \end{Bmatrix} \doteq \sum_{j=1}^N \begin{bmatrix} \boldsymbol{P}_{i,j} \\ \boldsymbol{P}_{i+1,j} \end{bmatrix} \overline{\boldsymbol{p}}_{G,j} = \sum_{j=1}^N \boldsymbol{R}_{\alpha,j} \overline{\boldsymbol{p}}_{G,j} \tag{37}$$

we finally obtain

$$V_\alpha^C = \sum_{j=1}^N \overline{\boldsymbol{p}}_{G,j}^\mathsf{T} b_\alpha \int_0^L (\boldsymbol{Y}_\alpha \boldsymbol{R}_{\alpha,j})^\mathsf{T} \boldsymbol{\omega}_\alpha \mathrm{d}X_1 = \sum_{j=1}^N \overline{\boldsymbol{p}}_{G,j}^\mathsf{T} \boldsymbol{g}_{\alpha,j}^C, \tag{38}$$

where $\boldsymbol{g}_{\alpha,j}^C$ is the vector of residual (internal) forces for interconnection α. Again, it should be noted that $\boldsymbol{Y}_\alpha$ in $\boldsymbol{g}_{\alpha,j}^C$ is dependent on $\boldsymbol{B}_\alpha$ and $\boldsymbol{\Lambda}_\alpha^m$ which, in contrast to [11], now depend on the unknown kinematic fields, thus introducing geometric non-linearity into the residual vector for the interconnection.

4. Solution procedure

From (25) and (38) total virtual work for a multi-layer beam with n layers and $n-1$ interconnections now reads

$$V^{TOT} = \sum_{i=1}^{n} \left[V_i^L + (1-\delta_{in}) V_i^C \right] = \sum_{j=1}^{N} \overline{\boldsymbol{p}}_{G,j}^{\mathsf{T}} \sum_{i=1}^{n} \left[\boldsymbol{g}_{i,j}^L + (1-\delta_{in}) \boldsymbol{g}_{i,j}^C \right], \quad (39)$$

where the same counter i is used for the layers and for the interconnections. Since the total virtual work of the multi-layer beam must equal zero ($V^{TOT} = 0$) and $\overline{\boldsymbol{p}}_{G,j}$ can be chosen arbitrarily, if follows that the nodal vector of residual forces for the multi-layer beam is

$$\boldsymbol{g}_j = \sum_{i=1}^{n} \left[\boldsymbol{g}_{i,j}^L + (1-\delta_{in}) \boldsymbol{g}_{i,j}^C \right] = \boldsymbol{q}_j^{int} - \boldsymbol{q}_j^{ext} = \boldsymbol{0}, \quad (40)$$

with

$$\begin{aligned} \boldsymbol{q}_j^{int} &= \sum_{i=1}^{n} \left(\int_0^L (\boldsymbol{D}_i \boldsymbol{P}_{i,j})^{\mathsf{T}} \boldsymbol{L}_i^{\mathsf{T}} \begin{Bmatrix} \boldsymbol{N}_i \\ M_i \end{Bmatrix} \mathrm{d}X_1 + (1-\delta_{in}) b_i \int_0^L (\boldsymbol{Y}_i \boldsymbol{R}_{i,j})^{\mathsf{T}} \boldsymbol{\omega}_i \mathrm{d}X_1 \right), \\ \boldsymbol{q}_j^{ext} &= \sum_{i=1}^{n} \left(\int_0^L \boldsymbol{P}_{i,j}^{\mathsf{T}} \begin{Bmatrix} \boldsymbol{f}_i \\ w_i \end{Bmatrix} \mathrm{d}X_1 + \boldsymbol{P}_{i,j}^{\mathsf{T}}(0) \begin{Bmatrix} \boldsymbol{F}_{i,0} \\ W_{i,0} \end{Bmatrix} + \boldsymbol{P}_{i,j}^{\mathsf{T}}(L) \begin{Bmatrix} \boldsymbol{F}_{i,L} \\ W_{i,L} \end{Bmatrix} \right), \quad (41) \end{aligned}$$

acting as the vectors of internal and external forces of the multi-layer beam, respectively. Expression (40) is highly non-linear in terms of the basic unknown parameters, thus the solution should be obtained numerically. To obtain the tangent stiffness matrix, the vector of residual forces has to be linearised. Since $\Delta \boldsymbol{q}_j^{ext} = \boldsymbol{0}$, only vector of the internal forces has to be linearised ($\Delta \boldsymbol{g}_j = \Delta \boldsymbol{q}_j^{int}$). For the layers, from (20) we have

$$
\begin{aligned}
\Delta \boldsymbol{D}_i &= \begin{bmatrix} \mathbf{0}_2 & -\hat{\boldsymbol{t}}_3 \Delta \boldsymbol{u}_i' \\ \mathbf{0}^\mathsf{T} & 0 \end{bmatrix}, \\
\Delta \boldsymbol{L}_i^\mathsf{T} &= \begin{bmatrix} \Delta\theta_i \hat{\boldsymbol{t}}_3 & \mathbf{0} \\ \mathbf{0}^\mathsf{T} & 0 \end{bmatrix} \boldsymbol{L}_i^\mathsf{T}, \\
\begin{Bmatrix} \Delta \boldsymbol{N}_i \\ \Delta M_i \end{Bmatrix} &= \boldsymbol{C}_i \begin{Bmatrix} \Delta \boldsymbol{\gamma}_i \\ \Delta \kappa_i \end{Bmatrix} = \boldsymbol{C}_i \boldsymbol{L}_i (\boldsymbol{D}_i \Delta \boldsymbol{p}_i),
\end{aligned}
\tag{42}
$$

where $\Delta \boldsymbol{D}_i$ and $\Delta \boldsymbol{L}_i$ come as a consequence of geometric non-linearity of the layers' deformation and $\mathbf{0}_2$ is 2×2 zero matrix. These terms do not exist in the procedure given in [11], and will result in the geometric stiffness matrix. For the interconnections, from (36) we have

$$
\begin{aligned}
\Delta \boldsymbol{Y}_i &= \hat{\boldsymbol{t}}_3 \left[\Delta \boldsymbol{\Lambda}_i^m (\boldsymbol{z}_i - s_i \boldsymbol{t}_{02}) + \boldsymbol{\Lambda}_i^m \Delta \boldsymbol{z}_i \right] \boldsymbol{\varphi}^\mathsf{T} + \Delta \boldsymbol{\Lambda}_i^m \boldsymbol{B}_i + \boldsymbol{\Lambda}_i^m \Delta \boldsymbol{B}_i, \\
\Delta \boldsymbol{\Lambda}_i^m &= \Delta\theta_i^m \hat{\boldsymbol{t}}_3 \boldsymbol{\Lambda}_i^m, \\
\Delta \boldsymbol{z}_i &= \boldsymbol{B}_i \Delta \boldsymbol{p}_{C,i}, \\
\Delta \boldsymbol{B}_i &= \begin{bmatrix} \mathbf{0}_2 & (h_i - a_i) \Delta\theta_i \boldsymbol{t}_{i,2} & \mathbf{0}_2 & a_{i+1} \Delta\theta_{i+1} \boldsymbol{t}_{i+1,2} \end{bmatrix}, \\
\Delta \boldsymbol{\omega}_i &= \boldsymbol{U}_i \Delta \boldsymbol{d}_i = \boldsymbol{U}_i \boldsymbol{Y}_i \Delta \boldsymbol{p}_{C,i},
\end{aligned}
\tag{43}
$$

where $\Delta \boldsymbol{\Lambda}_i^m$, $\Delta \boldsymbol{z}_i$ and $\Delta \boldsymbol{B}_i$ in $\Delta \boldsymbol{Y}_i$ come as a consequence of geometric non-linearity of the interconnection deformation. These terms do not exist in [11] and will contribute to the geometric stiffness matrix. Material non-linearity, in contrast is treated in the same manner as in [11], i.e.

$$\boldsymbol{U}_i = \begin{cases} \boldsymbol{S}_i & \text{if } \overline{\beta}_i \leq 0, \\ (\boldsymbol{I} - \boldsymbol{G}_i)\,\boldsymbol{S}_i & \text{if } \overline{\beta}_i > 0 \text{ and } \beta_i < \overline{\beta}_i, \\ (\boldsymbol{I} - \boldsymbol{G}_i)\,\boldsymbol{S}_i - \boldsymbol{J}_i \boldsymbol{S}_i \boldsymbol{d}_i \boldsymbol{v}_i^{\mathsf{T}} & \text{if } \overline{\beta}_i > 0 \text{ and } \beta_i = \overline{\beta}_i, \end{cases}$$

$$\Delta\boldsymbol{p}_{C,i} = \{\Delta\boldsymbol{p}_i \quad \Delta\boldsymbol{p}_{i+1}\}^{\mathsf{T}},$$

$$\boldsymbol{J}_i = \begin{bmatrix} \xi_{1,i} & 0 \\ 0 & \langle \operatorname{sgn}(d_{2,\alpha}) \rangle \xi_{2,i} \end{bmatrix}, \; \xi_{j,i} = \frac{d_{cj,i}}{d_{cj,i} - d_{0j,i}} \frac{\operatorname{sgn}(1 - g_{j,i})}{(1 + \overline{\beta}_i)^{\eta+1}}, \; j = 1, 2, \tag{44}$$

$$\boldsymbol{v}_i^{\mathsf{T}} = \left\langle \frac{1}{d_{1,i}} \left(\frac{|d_{1,i}|}{d_{01,i}} \right)^{\eta} \quad \frac{1}{d_{2,i}} \left(\frac{\langle d_{2,i} \rangle}{d_{02,i}} \right)^{\eta} \right\rangle.$$

Here it has to be emphasised that the third case (when $\overline{\beta}_i > 0$ and $\beta_i = \overline{\beta}_i$) in $\boldsymbol{U}_i$ is, in contrast to [11], now correctly derived. However, this error in linearisation did not cause any significant convergence problem in numerical examples presented in [11].

If we introduce $\begin{Bmatrix} \boldsymbol{n}_i \\ n_{i,3} \end{Bmatrix} = \boldsymbol{L}_i^{\mathsf{T}} \begin{Bmatrix} \boldsymbol{N}_i \\ M_i \end{Bmatrix}$, the layers' part of the linearised vector of residual forces becomes

$$\Delta\boldsymbol{g}_j^L = \sum_{i=1}^{n} \int_0^L \left\{ \boldsymbol{P}_{i,j}^{\mathsf{T}} \boldsymbol{Q}_i + (\boldsymbol{D}_i \boldsymbol{P}_{i,j})^{\mathsf{T}} \left[\boldsymbol{S}_i + \boldsymbol{L}_i^{\mathsf{T}} \boldsymbol{C}_i \boldsymbol{L}_i \boldsymbol{D}_i \right] \right\} \Delta\boldsymbol{p}_i \mathrm{d}X_1, \tag{45}$$

where

$$\boldsymbol{Q}_i = \begin{bmatrix} \boldsymbol{0}_2 & \boldsymbol{0} \\ -\boldsymbol{n}_i^{\mathsf{T}} \hat{\boldsymbol{t}}_3 \frac{\mathrm{d}}{\mathrm{d}X_1} & 0 \end{bmatrix}, \; \boldsymbol{S}_i = \begin{bmatrix} \boldsymbol{0}_2 & \hat{\boldsymbol{t}}_3 \boldsymbol{n}_i \\ \boldsymbol{0}^{\mathsf{T}} & 0 \end{bmatrix}, \tag{46}$$

which obviously depend on the current stress state and thus vanishes in the geometrically linear case. Since

$$\Delta\boldsymbol{p}_i = \begin{Bmatrix} \Delta\boldsymbol{u}_i \\ \Delta\theta_i \end{Bmatrix} = \sum_{k=1}^{N} \boldsymbol{\Psi}_k(X_1) \Delta\boldsymbol{p}_{i,k} = \sum_{k=1}^{N} \boldsymbol{P}_{i,k} \Delta\boldsymbol{p}_{G,k} \tag{47}$$

we can finally obtain

$$\Delta \boldsymbol{g}_j^L = \sum_{k=1}^{N} \boldsymbol{K}_{j,k}^L \Delta \boldsymbol{p}_{G,k}, \tag{48}$$

where

$$\boldsymbol{K}_{j,k}^L = \sum_{i=1}^{n} \int_0^L \left\{ \boldsymbol{P}_{i,j}^{\mathsf{T}} \boldsymbol{Q}_i \boldsymbol{P}_{i,k} + (\boldsymbol{D}_i \boldsymbol{P}_{i,j})^{\mathsf{T}} \boldsymbol{S}_i \boldsymbol{P}_{i,k} + (\boldsymbol{D}_i \boldsymbol{P}_{i,j})^{\mathsf{T}} \boldsymbol{L}_i^{\mathsf{T}} \boldsymbol{C}_i \boldsymbol{L}_i (\boldsymbol{D}_i \boldsymbol{P}_{i,k}) \right\} \mathrm{d}X_1 \tag{49}$$

is the nodal tangent stiffness block-matrix for all layers related to nodes j and k in which the first two terms make its geometric part, and the last term makes its material part. The interconnections' part of the linearised vector of residual forces reads

$$\Delta \boldsymbol{g}_j^C = \sum_{i=1}^{n-1} b_i \int_0^L \boldsymbol{R}_{i,j}^{\mathsf{T}} (\boldsymbol{\Omega}_i + \boldsymbol{Y}_i^{\mathsf{T}} \boldsymbol{U}_i \boldsymbol{Y}_i) \Delta \boldsymbol{p}_{C,i} \mathrm{d}X_1, \tag{50}$$

where

$$\begin{aligned} \boldsymbol{\Omega}_i &= \varphi \boldsymbol{\omega}_i^{\mathsf{T}} \hat{\boldsymbol{t}}_3 \boldsymbol{Y}_i + (\boldsymbol{\Lambda}_i^m \boldsymbol{B}_i)^{\mathsf{T}} (\varphi \boldsymbol{\omega}_i^{\mathsf{T}} \hat{\boldsymbol{t}}_3)^{\mathsf{T}} + \boldsymbol{Z}_i, \\ \boldsymbol{Z}_i &= \begin{bmatrix} \boldsymbol{0}_2 & \boldsymbol{0} & \boldsymbol{0}_2 & \boldsymbol{0} \\ \boldsymbol{0}^{\mathsf{T}} & (h_i - a_i)(\boldsymbol{\Lambda}_i^m \boldsymbol{t}_{i,2})^{\mathsf{T}} \boldsymbol{\omega}_i & \boldsymbol{0}^{\mathsf{T}} & 0 \\ \boldsymbol{0}_2 & \boldsymbol{0} & \boldsymbol{0}_2 & \boldsymbol{0} \\ \boldsymbol{0}^{\mathsf{T}} & 0 & \boldsymbol{0}^{\mathsf{T}} & a_{i+1}(\boldsymbol{\Lambda}_i^m \boldsymbol{t}_{i+1,2})^{\mathsf{T}} \boldsymbol{\omega}_i \end{bmatrix}, \end{aligned} \tag{51}$$

which vanish in the geometrically linear case owing to the presence of current interconnection tractions $\boldsymbol{\omega}_i$. Considering that

$$\Delta \boldsymbol{p}_{C,i} = \sum_{k=1}^{N} \boldsymbol{R}_{i,k} \Delta \boldsymbol{p}_{G,k}, \tag{52}$$

we finally obtain

$$\Delta \boldsymbol{g}_j^C = \sum_{k=1}^{N} \boldsymbol{K}_{j,k}^C \Delta \boldsymbol{p}_{G,k}, \tag{53}$$

where

$$\boldsymbol{K}^{C}_{j,k} = \sum_{i=1}^{n-1} \int_{0}^{L} (\boldsymbol{R}^{\mathsf{T}}_{i,j} \boldsymbol{\Omega}_i \boldsymbol{R}_{i,k} + \boldsymbol{R}^{\mathsf{T}}_{i,j} \boldsymbol{Y}^{\mathsf{T}}_{i} \boldsymbol{U}_i \boldsymbol{Y}_i \boldsymbol{R}_{i,k}) \mathrm{d}X_1 \tag{54}$$

is the nodal tangent stiffness block-matrix for all interconnections related to nodes j and k. The first term represents its geometric part, while the second term represents its material part. Since $\Delta \boldsymbol{g}_j = \Delta \boldsymbol{g}^{L}_{j} + \Delta \boldsymbol{g}^{C}_{j}$, it follows that the total nodal tangent stiffness block-matrix for a multi-layer beam composed of n layers and $n-1$ interconnections related to nodes j and k can be computed as

$$\boldsymbol{K}_{j,k} = \boldsymbol{K}^{L}_{j,k} + \boldsymbol{K}^{C}_{j,k}. \tag{55}$$

On the element level, the vector of residual forces, the tangent stiffness matrix and the vector of increments of unknown parameters are assembled as in [11], while their global counterparts $\boldsymbol{g}$, $\boldsymbol{K}$ and $\Delta \boldsymbol{p}$ are assembled using the standard finite-element procedure [19]. The following equations are then repeatedly solved and the unknown parameters, stress resultants and interconnection tractions, and the internal force vectors updated until satisfying accuracy is achieved:

$$\Delta \boldsymbol{p} = -\boldsymbol{K}^{-1} \boldsymbol{g}, \tag{56}$$

i.e. using the Newton-Raphson method. For integration in (41), (49) and (54) we use Gauss quadrature with $N-1$ points for the layers and Simpson's rule with 3 points for the interconnections (for additional information about numerical integration for the interconnections see [10]).

Solution algorithm has been implemented within the computer package *Wolfram Mathematica*. For the geometrically linear problems presented in [11] the solution path is obtained using the modified arc-length procedure [10], which, unlike the standard arc-length procedure, was able to overcome the sharp snap-backs which eventually occur in the load displacement diagram. However, the procedure sometimes returned to previously obtained equilibrium states ("back-

tracking") which was overcome by not taking into account solutions that close a very sharp angle with the previously obtained equilibrium path, and reducing the arc-length. If after a certain number of arc-length reductions the convergence to a satisfactory solution still was not obtained, the arc-length would be then repeatedly increased. In general, we assumed that the procedure has converged to a solution when the norm of the residual vector is smaller than a pre-defined tolerance, i.e. $|\boldsymbol{g}| < tol$. In all numerical examples presented in the present work $tol = 10^{-4}$.

For the geometrically non-linear problems, obtaining the equilibrium path using the same method as for the geometrically linear problems has often proven to be more difficult and sometimes impossible. This has served as the motivation to propose a new, more robust method, which is based on the principle that the total damage of the system in delamination problems can only increase (in the case of ongoing delamination) or at least remain unchanged (when delamination process has not started, is interrupted or it is over) with each new load step. To measure the total delamination of the system a "total damage" parameter

$$g_{TOT} = \sum_{\alpha=1}^{n-1} \sum_{el=1}^{N_e} \sum_{s=1}^{N_s} g_{\alpha}^{m}(el, s) \tag{57}$$

is introduced, where for an element el and a Simpson's integration point s, $g_{\alpha}^{m}(el, s)$ takes the mean value between the mode I and mode II damage as

$$g_{\alpha}^{m}(el, s) = \frac{g_{1,\alpha}(el, s) + g_{2,\alpha}(el, s)}{2}. \tag{58}$$

According to (32), $g_{i,\alpha}(el, s)$, $i = 1, 2$, can take values between 0 and 1, where 0 means no damage, while 1 represents the total damage. Thus, when total damage is reached in both directions (total mixed-mode delamination) in an element n and Simpson's integration point s, we have $g_{\alpha}^{m}(el, s) = 1$.

In this new, damage-based arc-length procedure, at the start of an analysis $g_{TOT} = 0$ and the solution algorithm uses the standard arc-length procedure until the value of g_{TOT} is changed at the beginning of a load step. Then, since the damage process has obviously started, a new method of choosing the correct

root $\delta\lambda$ of the arc-length quadratic equation is used (see [20, 21] for more detail about this issue with standard and modified arc-length procedure). This new method first checks if al least one root of the quadratic arc-length equation gives g_{TOT} which is greater than the g_{TOT} from the previous load step. If this is not the case, which means that there is no increase in the total damage of the system, the standard arc-length procedure is used. If there is only one $\delta\lambda$ which gives g_{TOT} greater than the one from the previous load step, this $\delta\lambda$ is taken to be the correct root as the one which gives the increase of the total damage of the system. In case when both roots of the arc-length quadratic equation give solutions which result in an increase in the total damage of the system, the correct root is taken to be the one which gives smaller norm of the residual vector (similar as in the modified arc-length method).

Independent of the method used (standard or the new damage-based arc-length procedure) the arc-length size can be assigned as constant, with occasional reductions when the convergence cannot be achieved, or adaptive, defined by the following equation:

$$c(i) = \sqrt{\frac{N_{it}^{d}}{N_{it}(i-1)}}\, c(i-1), \tag{59}$$

where $c(i)$ is the arc-length size in the current load step i, N_{it}^{d} is the desired number of iterations (which is defined at the start of an analysis), $N_{it}(i-1)$ is the number of iterations needed to obtain convergence in the previous load step $i-1$ and $c(i-1)$ is the arc-length size from the previous load step. If the convergence is not obtained after a pre-defined maximum number of iterations N_{it}^{max}, the load step is repeated with a reduced arc length $c^{r}(i) = \mu_1 c^{r-1}(i)$, where r is the ordinal number of the load-step repetition, $c^{0}(i) := c(i)$ and $\mu_1 < 1$ is an arc-length reduction factor. If after a pre-defined maximum number of arc-length reductions N_{red}^{max} there is still no convergence, the arc-length is set to a new, larger value $c_j(i) = \mu_2 c_{j-1}(i)$, where j is the ordinal number of the load-step repetition with an arc-length increase and $\mu_2 > 1$ is an arc-length augmentation coefficient, and the procedure with arc-length reductions is repeated again for a

pre-defined maximum number of arc-length increases N_{aug}^{max}. In the numerical examples presented in the present paper $\mu_1 = 0.5$ and $\mu_2 = 1.25$ are used.

5. Numerical examples

5.1. Single mixed-mode delamination

In this example, a so-called "end-notch flexure" (ENF) specimen is simply supported and loaded with two forces $F_1 = 0.4535F_2$ and F_2 causing the mixed-mode delamination at the interconnection as shown in Fig. 5. This numerical test was proposed by Mi *et al.* [3] and also analysed in our previous work [11], where the geometrically linear model was used.

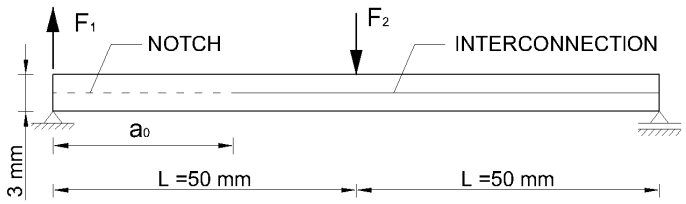

Figure 5: End-notch flexure specimen for mixed-mode delamination

Geometrical properties of the specimen are shown in Fig. 5, with width of the beam $b_i = 1$ mm ($i = 1, 2$, the beam is modelled as two-layered) and the notch length $a_0 = 30$ mm. Since the material properties for the bulk material in [3] were given for the orthotropic material (two Young's moduli, one shear modulus and two Poisson's coefficients), in [11], as well as in the present work, only Young's modulus in the longitudinal direction and the shear modulus in the corresponding transverse direction are used and given as $E_i = 135300$ N/m^2 and $G_i = 5200$ N/mm^2, $i = 1, 2$, respectively. The material properties for the interconnection are $\omega_{0j} = 57$ N/mm^2, $d_{0j} = 10^{-7}$ mm, $d_{cj} = 0.14$ mm and $S_j = 5.7 \cdot 10^8$ N/mm^3, $j = 1, 2$. In this example, the damage-based arc-length procedure presented in Section 4 is used with adaptive arc-length and $c(0) = 10^{-3}$, $N_{it}^{d} = 15$, $N_{it}^{max} = 25$, $N_{red}^{max} = 10$, $N_{aug}^{max} = 10$. The reference

axes of both layers are positioned at the plane of the interconnection ($a_1 = h_1$ and $a_2 = 0$) and 80 equal linear two-layer beam finite elements are used.

Since in our previous work [11] we noted that the displacements at the end of the equilibrium path reported in [3] considerably exceeded the limit of small displacements and rotations (displacements up to 40% of the total length of the beam), we have found quite interesting to investigate if the use of geometrically exact formulation has any significant influence on the results. In fact, the differences are very pronounced, as can be noticed in Fig. 6, where the displacements of the reference axis of the upper layer at the left-hand end obtained by both the geometrically linear and the geometrically non-linear formulation are plotted. It should be noticed that, in contrast to the geometrically linear formulation, in the geometrically exact formulation the horizontal displacement of the free end of the upper layer also exists and even for the range of loading values in [3, 11] takes considerable values (cca 20% of the value of the vertical displacement for $F_1 = 20$ N).

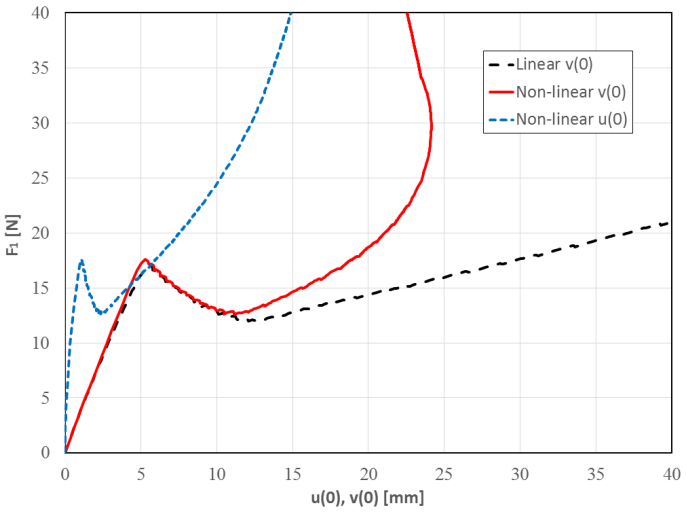

Figure 6: Results for the mixed-mode delamination test on the ENF specimen obtained using both geometrically linear and non-linear multi-layer beam models

Fig. 6 shows only a part of the diagram which we obtain using the geometrically exact model for which $F_1 \equiv 0.4535F_2 \leq 40$N. If we continue to increase the forces F_1 and F_2 further, the system behaves as shown in Fig. 7. It can be observed that the force F_1 reaches the peak at about 136 N, but the vertical displacement never reaches 40 mm shown in Fig. 6 as obtained for the geometrically linear case. In contrast to the geometrically linear analysis, in geometrically non-linear analysis the distance between forces F_1 and F_2 reduces as they increase. The force F_2 causes bending of the beam, while the force F_1 is responsible for the mixed-mode delamination at the interconnection. It is very important to note that in the geometrically linear case the bending moment in the upper layer at the mid-span is equal to F_1L, whereas in the geometrically non-linear case it gets progressively smaller than F_1L as the loading increases. For this reason, in the latter case the vertical displacement of the left-hand end of the upper layer necessarily becomes bounded, and so does the mode 1 crack propagation, too. After the crack reaches the midspan, a significant increase in the force F_1 is needed to obtain further delamination progress and the left-hand side end of the upper layer is actually decreasing as the midspan deflection of the whole beam increases. In Fig. 7 can be also noted that the right-hand side support slides and approaches the left-hand side support as the beam deforms, reducing the span of the beam. It can be concluded that this example, which is often reported in the literature, has to be treated as geometrically non-linear, especially when the vertical displacement at the free end of the upper layer exceeds cca 10% of the total beam length (see Fig. 6).

5.2. Double mixed-mode delamination

This example, first proposed by Robinson *et al.* [22] and later investigated by Alfano & Crisfiled [10, 23], was also reported in our previous work [11], where we obtained an excellent agreement of the results using significantly less degrees of freedom. The original HTA913 specimen is originally made of 24 layers of equal thickness, but since the connections between all layers are assumed to be rigid wherever they exist, the structure is modelled as a three-layer beam

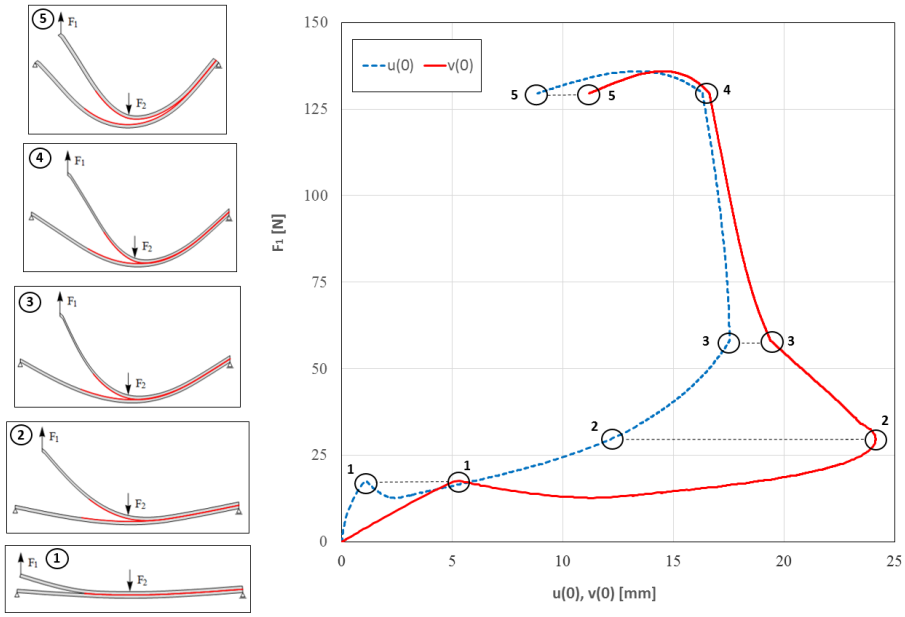

Figure 7: Behaviour of the ENF specimen under large displacements and rotations

with two interconnections in the planes where the initial cracks are positioned and expected to propagate. Fig. 8 shows the geometry of the specimen, where $h_1 = 1.325$ mm, $h_2 = 0.265$ mm, $h_3 = 1.59$ mm and width $b_i = 20$ mm, $i = 1, 2, 3$ (note different length and height scales in Fig. 8). The reference axes of all layers coincide with their centroidal axes, i.e. $a_i = 0.5h_i$, $i = 1, 2, 3$. The support at the bottom of the left-hand side keeps the bottom layer fixed (allowing only rotation), while the upper layer can slide in only the vertical direction under the load F. As it was reported in [11], as the force F increases, first the upper crack propagates and, when the horizontal position of its tip reaches the bottom crack, both cracks continue to propagate simultaneously. It was also noticed that, before it starts to propagate, compressive contact tractions occur at the bottom crack.

The orthotropic material properties for HTA913 given in [22] are adapted for the beam model as $E_i = 115.0$ GPa, $G_i = 4.5$ GPa, $(i = 1, 2, 3)$, whereas for the interconnection, according to [23] three sets of material properties are used

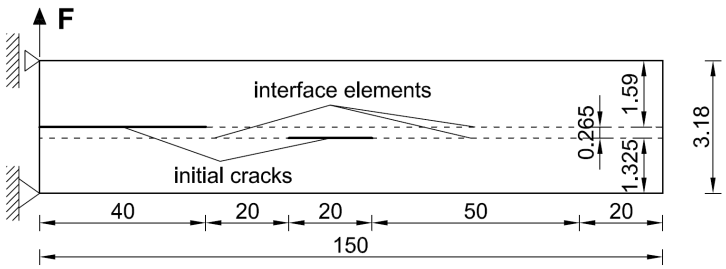

Figure 8: Double mixed-mode delamination specimen (all dimensions are in mm)

(see Table 1).

Table 1: Material properties of the interconnection for the double mixed-mode delamination example

Case	$G_{c1,\alpha}$ [N/mm]	$G_{c1,\alpha}$ [N/mm]	$d_{0j,\alpha}/d_{cj,\alpha}$	$\omega_{01,\alpha}$ [MPa]	$\omega_{02,\alpha}$ [MPa]	$d_{0j,\alpha}$ [mm]	$d_{cj,\alpha}$ [mm]	$S_{1,\alpha}$ [N/mm^3]	$S_{2,\alpha}$ [N/mm^3]
A	0.8	0.33	$5{\cdot}10^{-5}$	8.0	3.3	$1{\cdot}10^{-5}$	0.2	$8{\cdot}10^{5}$	$3.3{\cdot}10^{5}$
B	0.8	0.33	$1.25{\cdot}10^{-3}$	40.0	16.5	$5{\cdot}10^{-5}$	0.04	$8{\cdot}10^{5}$	$3.3{\cdot}10^{5}$
C	0.8	0.33	$5{\cdot}10^{-3}$	80.0	33.0	$1{\cdot}10^{-4}$	0.02	$8{\cdot}10^{5}$	$3.3{\cdot}10^{5}$

The meshing is this example is performed as in [11], where two different meshes of quadratic three-layer beam finite elements are used: mesh 1 for material case A and mesh 2 for material cases B and C (see Table 2).

Table 2: Finite-element meshes for the double mixed-mode delamination example with different material properties for the interconnection

	Zone 1	Zone 2	Zone 3	Zone 4	Zone 5	Total
Length [mm]	40	20	20	50	20	150
Initial crack	$\alpha = 2$	none	$\alpha = 1$	none	none	
Mesh 1 / No. of FE	2	20	20	50	5	97
Mesh 2 / No. of FE	4	40	40	100	5	189

In the numerical simulations for both the geometrically linear and nonlinear analysis a constant arc-length $c = 5$ is used with occasional reductions ($\mu_1 = 0.5$), while the maximum number of iteration N_{it}^{max}, the maximum num-

ber of arc-length reductions N_{red}^{max} and the maximum number of arc-length augmentations N_{aug}^{max} are set to $N_{it}^{max} = 50$, $N_{red}^{max} = 15$ and $N_{aug}^{max} = 10$. To reach the value of the vertical displacement of the left-hand end of the upper layer $v_3(0) = 35$ mm (see Figs. 9-11) we need 193, 326 and 510 load steps for the geometrically linear analysis, and 318, 518 and 1426 load steps for the geometrically non-linear analysis, respectively for the cases A, B and C. Using the above arc-length, the algorithm jumps over certain parts of the load-displacement diagram (including spurious oscillations) without losing convergence, but many times the arc-length has had to be reduced (one or more times) in order to obtain convergence. Every reduction of the arc-length basically increases the number of the load steps needed to complete the analysis and there are more reductions in the geometrically non-linear analysis. From Figs. 9-11 we can note that spurious oscillations for cases B and C are larger than for the case A, although the FE meshes used for cases B and C are twice denser than the one used for the case A. This means that the material model of the interconnection has more influence on the spurious oscillations than the finite-element length itself (see Tabs. 1 and 2). Obviously, larger oscillations demand more load steps because the total length of the equilibrium path is longer (especially for the case C). However, in comparison with the geometrically linear analysis, the spurious oscillations for each case are smaller.

The results of the multi-layer beam model for the geometrically linear analysis for this example have been already compared with the results from the literature (see [11] for details) where it was concluded that the the presented model gives comparable accuracy using significantly less degrees of freedom. In this work we further analyse how the introduction of geometrical non-linearity affects the results in this example where the displacements and rotations are not small and the problem itself is rather complex (irregular positions of the initial cracks, non-symmetric layering). For all three sets of the material parameters for the interconnection, the difference between the geometrically linear and non-linear analysis is more pronounced for the parts of the diagram where the bottom

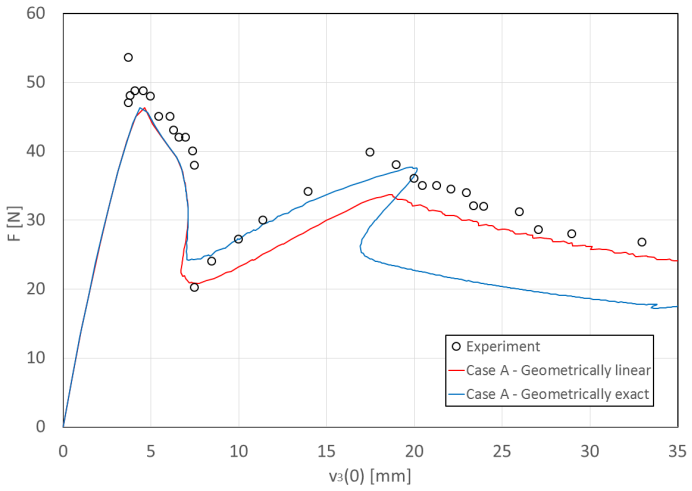

Figure 9: Applied force F against the vertical displacement of the left-hand side of the upper layer $v_3(0)$ for the case A of the material parameters

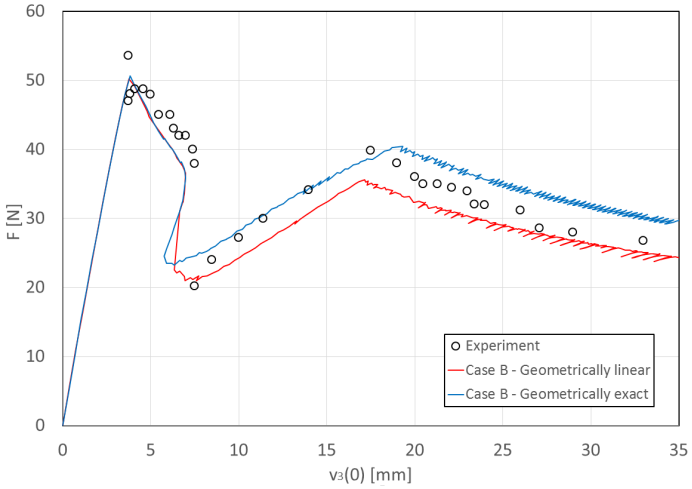

Figure 10: Applied force F against the vertical displacement of the left-hand side of the upper layer $v_3(0)$ for the case B of the material parameters

initial crack has propagated (the part with $v_3(0)$ in the region from cca. 7 to 35 mm). In addition, only for the case A the equilibrium path after $v_3(0) \approx 19$ mm in the geometrically non-linear analysis is quite different in comparison not only to that in the geometrically linear analysis, but to the experiment as well.

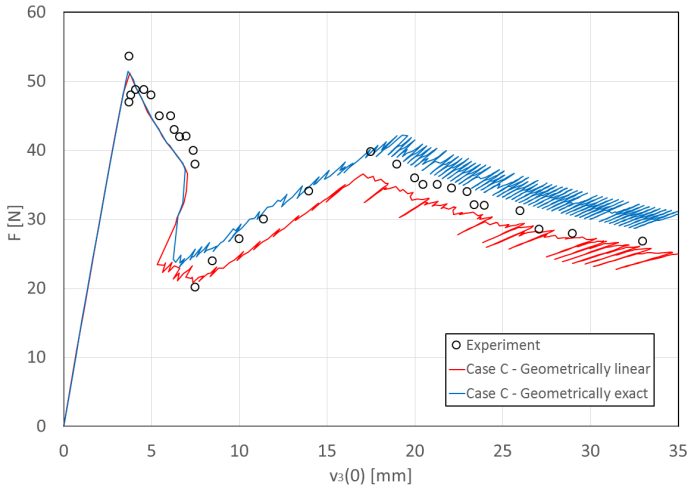

Figure 11: Applied force F against the vertical displacement of the left-hand side of the upper layer $v_3(0)$ for the case C of the material parameters

The exact kinematic equations (10) and the new definition of the directions for the delamination modes I and II (26)-(28), in combination with the material parameters of the interconnection, for the case A result in a behaviour where the bottom initial crack for $v_3(0)$ between cca. 7 and 19 mm opens and then closes again, but does not continue to propagate to the right-hand side for larger values of $v_3(0)$ (only the upper crack continues to propagate). Using a denser mesh (Mesh 2 from Table 2) for the case A gives exactly the same behaviour (not shown). Obviously, the material properties of the interconnection given for the case A do not model the real behaviour obtained by the experiment accurately. In contrast to the geometrically linear analysis, the overall results of which have turned out to be largely insensitive to the variation of the material properties of the interconnection described by the cases A, B and C, in the geometrically non-linear analysis this can be asserted only for the variation of the material parameters lying int the range defined by the cases B and C. We can conclude that in this example the case B is the most suitable both in geometrically linear and non-linear analysis because of its rather good agreement with the experimental results and acceptable size of the spurious oscillations (although Mesh

2 is used). In addition, it is useful to note that for the range of values of $v_3(0)$ between cca. 7 and 35 mm the actual response of the specimen lies between the predictions of the linear and the non-linear analysis for both case B and case C.

5.3. Buckling of a double-cantilever beam

Allix and Corigliano [24] proposed an example where the layers of a double-cantilever beam (DCB) were loaded by two compressional axial forces which caused buckling of the layers and crack propagation along the interconnection (see Fig. 12). The width of the specimen was $b = b_i = 1$ mm and the material properties for the layers read $E_i = 135000$ N/mm^2 and $G_i = 5700$ N/mm^2, $i = 1, 2$. Two perturbational forces $F_0 = 0.001$ N were applied on each layer to induce the buckling in the desired direction. Since the geometrical and material properties of the layers, as well as the applied loading, were symmetric with respect to the plane of interconnection, pure mode I delamination occurred as the initial cracks began to propagate. For the interconnection, the following material parameters were given: $S_1 = 10^6$ N/mm^3, $\omega_{01} = 50$ N/mm^2 and a set of fracture energies $G_{c,1} = \{0.2, 0.4, 0.8, 1.6\}$ N/mm with the corresponding separations at the complete damage $d_{c,1} = \{0.008, 0.016, 0.032, 0.064\}$ mm. No data regarding the FE mesh used in the analysis were given in [24].

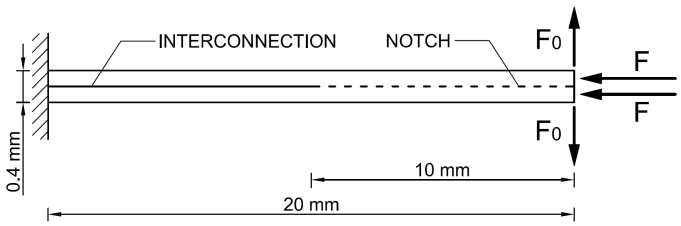

Figure 12: Specimen for buckling in a DCB

The example is here run using the proposed algorithm, where first the forces F_0 are applied to obtain the initial deformed configuration and then the damage-based modified arc-length procedure is applied (as presented in Section 4), where only the load F is variable, while F_0 is kept constant. After the first load step,

where arc-length is $c(1) = 0.001$, the arc-length is changed in each load step according to (59) with $N_{it}^{d} = 15$, $N_{it}^{max} = 25$, $N_{red}^{max} = 10$, $N_{aug}^{max} = 10$, $\mu_1 = 0.75$, $\mu_2 = 1.5$ and a constraint $c(i) \leq 2$, $i > 1$. 200 linear two-layer beam finite elements are used in the analysis, where the reference axes of each layer coincide with their centroidal axes ($a_i = 0.5h_i$, $i = 1, 2$) in order to avoid eccentricity of the axial loads.

The present model, where the exact geometrical non-linearity is accounted for, is compared to the model presented by Allix and Corigliano [24], where geometrical non-linearity is introduced in a multi-layer beam model only as an influence of transversal displacements on axial strains (the second-order theory). In Fig. 13, where the displacement of the free end of the upper layer $v_2(L)$ is plotted against the applied force F, for both cases we can observe the same behaviour at the beginning of the process, where we have an almost vertical line (very small change of displacement with increasing the load F) before reaching the buckling force somewhere around 2 N. After the buckling has started it can be noticed that the displacement rapidly increases with a slowly increasing force F. At a certain point, depending on the material properties of the interconnection, the buckling deformation of individual layers damages the interconnection, which is presented by the softening branches in Fig. 13. There is also a graph presenting how the system would behave if the interconnection were completely rigid ($G_c = \infty$), where it can be noted that the non-physical displacement $v_2(L) \geq 10$ mm, obtained by the model presented in [24], cannot be obtained using the geometrically exact formulation presented in this work even for $F > 3$ N. The differences between the two models, as expected, are more pronounced for larger displacements, especially in the case where the interconnection is completely rigid.

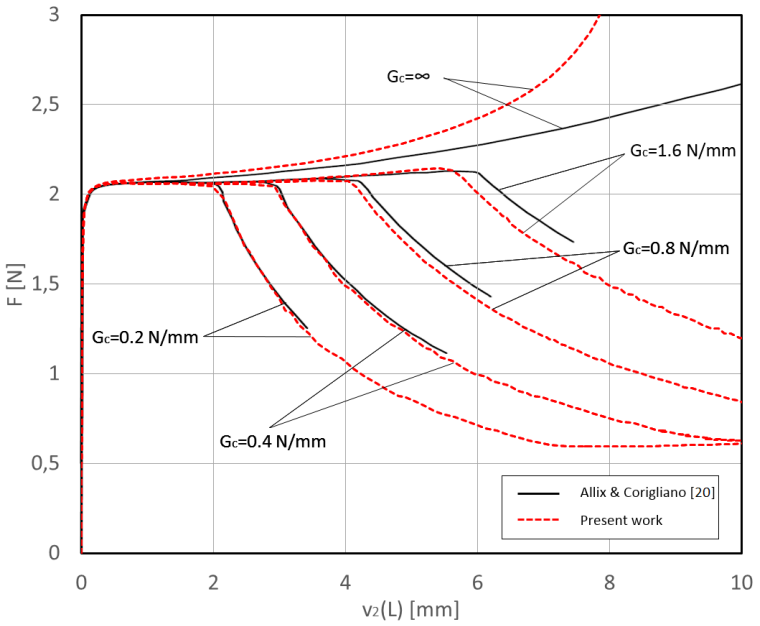

Figure 13: Comparison of the results for the buckling of the DCB specimen

6. Conclusions and future work

In this work we have proposed a geometrically exact multi-layer beam finite element formulation with interconnection allowing for mixed-mode delamination. The formulation is given in a general form where the number of layers and nodes of the beam finite elements is arbitrary, as well as the geometrical parameters for the layers and the interconnections, while the constitutive laws are assumed to be linear elastic for the layers and a bi-linear mixed-mode damage law for the interconnection. In order to solve numerical problems that are, due to the introduction of the exact kinematic equations, more complex and numerically demanding, we have proposed a new modification of the arc-length method, where the standard arc-length procedure is used only when there is no damage at the interconnection, else in each load step the converged solution has to result in an increase in the total damage of the system. In the numerical examples, we have shown that using the geometrically linear formulation in cases when the displacements of the system are moderate to large can lead to

significant differences in the results. On the other hand, for examples that can be solved using only geometrically non-linear formulations (e.g. DCB buckling in Section 5.3), we have shown that the proposed geometrically exact formulation gives significant differences in the results compared to the second-order beam theory in the post-critical region. Since the presented geometrically exact formulation is more accurate, gives considerable differences in the results and is not significantly computationally expensive than the other formulations used in our comparisons, it can be successfully applied to all types of planar delamination problems. The geometrically linear formulations, as shown in the examples presented in the present work, can be used with satisfactory accuracy only in limited number of cases where displacements and rotations remain small.

The presented model will be further developed by introducing rate-dependence into the interface's cohesive law (see [25] and [26]). Other developments may include the introduction of material non-linearity (such as plasticity or hyper-elasticity) in the layers and application of some higher-order beam theories which would allow warping of the layers' cross-sections and non-linear stress distribution over layers' height. It is also possible to introduce layers with deformable thickness where strains and stresses transverse to layer's reference axes appear (see [27] for application in multi-layer beams with rigid interconnection).

Acknowledgement

These results were obtained within the research project No IP-11-2013-1631 (Configuration-dependent approximation in non-linear finite-element analysis of structures) financially supported by the Croatian Science Foundation. We also acknowledge the University of Rijeka financial support for ongoing research No 13.05.1.3.06 (Testing of slender spatial beam structures with emphasis on model validation).

References

[1] Z. Bažant, L. Cedolin, Stability of Structures, Dover, 2003.

[2] A. A. Griffith, The phenomena of rupture and flow in solids, Philosophical Transactions of the Royal Society of London A 221 (1921) 163–198.

[3] Y. Mi, M. A. Crisfield, G. A. O. Davies, H. B. Hellweg, Progressive delamination using interface elements, Journal of Composite Structures 32 (14) (1998) 1246–1272.

[4] T. L. Anderson, Fracture Mechanics: Fundamentals and Applications, Third Edition, CRC Press, Boca Ranton, Florida, USA, 2005.

[5] G. I. Barenblatt, The formation of equilibrium cracks during brittle fracture - general ideas and hypothesis, axially symmetric cracks, Journal of Applied Mathematics and Mechanics 23 (3) (1959) 622–636.

[6] J. Oliver, A. Huespe, M. Pulido, E. Chaves, From continuum mechanics to fracture mechanics: the strong discontinuity approach, Engineering Fracture Mechanics 69 (2002) 113–136.

[7] A. Hillerborg, M. Modéer, P. E. Petersson, Analysis of crack formation and crack growth in concrete by means of fracture mechanics and finite elements, Cement and Concrete Research (Sec. 12.2) 6 (1976) 773–782.

[8] M. Elices, G. Guinea, J. Gómes, J. Planas, The cohesive zone model: advantages, limitations and challenges, Engineering Fracture Mechanics 69 (2002) 137–163.

[9] R. de Borst, Fracture in quasi-brittle materials: a review of continuum damage-based approaches, Engineering Fracture Mechanics 69 (2002) 95–112.

[10] G. Alfano, M. A. Crisfield, Finite element interface models for the delamination analysis of laminated composites: mechanical and computational issues, International Journal for Numerical Methods in Engineering 50 (7) (2001) 1701–1736.

[11] L. Škec, G. Jelenić, N. Lustig, Mixed-mode delamination in 2D layered beam finite elements, International Journal for Numerical Methods in Engineering 104 (2015) 767–788.

[12] L. Škec, G. Jelenić, Analysis of a geometrically exact multi-layer beam with a rigid interlayer connection, Acta Mechanica 225 (2) (2014) 523–541.

[13] L. Vu-Quoc, H. Deng, Galerkin projection for geometrically exact sandwich beams allowing for ply drop-off, Journal of Applied Mechanics 62 (1995) 479–488.

[14] L. Vu-Quoc, I. K. Ebcioğlu, General multilayer geometrically-exact beams and 1-d plates with piecewise linear section deformation, Journal of Applied Mathematics and Mechanics (ZAMM) 76 (7) (1996) 391–409.

[15] E. Reissner, On one-dimensional finite-strain beam theory; the plane problem, Journal of Applied Mathematics and Physics (ZAMP) 23 (5) (1972) 795–804.

[16] J. C. Simo, L. Vu-Quoc, On the dynamics of flexible beams under large overall motions - the plane case: Part i and ii, Journal of Applied Mechanics 53 (4) (1986) 849–863.

[17] G. R. Cowper, The shear coefficient in Timoshenko's beam theory, Journal of Applied Mechanics 33 (2) (1966) 335–340.

[18] A. Kroflič, M. Saje, I. Planinc, Non-linear analysis of two-layer beams with interlayer slip and uplift, Computers & Structures 89 (23-24) (2011) 2414–2424.

[19] O. C. Zienkiewicz, R. L. Taylor, J. Z. Zhu, The Finite Element Method. Its Basis & Fundamentals, Butterworth-Heinemann, Oxford, UK, 2005.

[20] L. Škec, Non-linear static analysis of multilayered 2d beams with various contact conditions between layers, Ph.D. thesis, University of Rijeka, Faculty of Civil Engineering (2014).

[21] M. A. Crisfield, Non-Linear Finite Element Anaylsis of Solids and Structures, Vol. 1, Wiley, Chichester, England, 1996.

[22] P. Robinson, T. Besant, D. Hitchings, Delamination growth prediction using a finite element approach, in: J. Williams, A. Pavon (Eds.), Fracture of Polymers, Composites and Adhesives, Elsevier, Amsterdam, 2000, pp. 135–147.

[23] G. Alfano, M. A. Crisfield, Solution strategies for the delamination analysis based on a combination of local-control arc-length and line searches, International Journal for Numerical Methods in Engineering 58 (2003) 999–1048.

[24] O. Allix, A. Corigliano, Geometrical and interfacial non-linearities in the analysis of delamination in composites, International Journal of Solids and Structures 36 (1999) 2189–2216.

[25] M. Musto, G. Alfano, A novel rate-dependent czm combining damage and visco-elasticity, Composite Structures 118 (2013) 126–133.

[26] M. Musto, G. Alfano, A fractional rate-dependent cohesive-zone model, International Journal for Numerical Methods in Engineering 105 (5) (2015) 313–341.

[27] L. Vu-Quoc, I. K. Ebcioğlu, General multilayer geometrically-exact beams and one-dimensional plates with deformable layer thickness, Journal of Applied Mathematics and Mechanics (ZAMM) 80 (2) (2000) 113–135.